ADVANCED FUNCTIONAL MATERIALS
www.afm-journal.de

Ultrathin Metal Fluoride Interfacial Layers for Use in Organic Photovoltaic Cells

Fengyuan Lin, Xingyuan Liu, Yantao Li, Yongsheng Hu, and Xiaoyang Guo**

A variety of metal fluorides, including lithium fluoride (LiF), magnesium fluoride (MgF_2), barium fluoride (BaF_2), strontium fluoride (SrF_2), aluminum fluoride (AlF_3), zirconium fluoride (ZrF_4), and cerium fluoride (CeF_3), are used as the cathode interfacial layer (CIL) in polymer photovoltaic cells to assess their effect on device performance. CeF_3, BaF_2, and SrF_2 CILs exhibit better performance than a typical LiF CIL. The SrF_2-based device shows a power conversion efficiency (PCE) of 7.17%, which is approximately 9% higher than that of the LiF-based device; this, to our knowledge, is the first report on the SrF_2-based organic photovoltaic cell device. The open-circuit voltage (V_{OC}) and fill factor (FF) of the fluoride-based devices are correlated to the work functions (WFs) of the corresponding metals, which in turn influence the PCE. X-ray photoelectron spectroscopy measurements of fluoride-based cathodes reveal the occurrence of a displacement reaction and an interfacial dipole at the fluoride/aluminum interface, which lead to a reduced effective WF of the cathode and improved charge collection. Consequently, an improved PCE is achieved together with an increased V_{OC} and FF.

1. Introduction

Over the past few years, organic photovoltaic cells (OPVs) prepared from blends of conjugated polymers and fullerene derivatives have received increasing attention because of their flexibility, renewability, low cost, and environment-friendliness.[1–10] Recently, the power conversion efficiency (PCE) of single-layer bulk-heterojunction polymer solar cells has been reported to exceed 10% as a result of the integrated innovative material design.[11–13] To realize high PCE, the following factors are essential: a small bandgap donor to harvest the major fraction of solar photons, good morphology of the active layer for efficient charge generation and transport, electrodes with suitable work functions (WFs) for formation of ohmic contacts, and the maximum built-in electric field to facilitate charge extraction.

Dr. F. Lin, Prof. X. Liu, Dr. Y. Li, Dr. Y. Hu, Dr. X. Guo
State Key Laboratory of Luminescence and Applications
Changchun Institute of Optics
Fine Mechanics and Physics
Chinese Academy of Sciences
Changchun 130033, P.R. China
E-mail: liuxy@ciomp.ac.cn; guoxy@ciomp.ac.cn
Dr. F. Lin
University of Chinese Academy of Sciences
Beijing 100039, P.R. China

DOI: 10.1002/adfm.201502871

To realize efficient electron transport and extraction, low-WF electrodes, such as alkali and alkaline earth metals (Ca, Mg, Ba, etc.), are usually required. However, low-WF metals are easily oxidized and chemically reactive in ambient atmosphere, which affects the stabilities of the electrodes and devices.[14,15] Therefore, different types of buffer layers, such as dipole polymer PHS,[16] transition metal oxides TiO_x, ZnO, and V_2O_x,[17–23] are used to lower the WFs of electrodes and improve stability. However, the devices containing these oxide interface layers suffered from the "light-soaking" problem; that is, they exhibited hysteresis phenomena under continuous illumination, which resulted in fluctuations in device performance.[24,25] To prevent the oxidation of reactive metals to insulating metal oxides, and hence enhance the device lifetime, ultrathin metal fluorides with low WFs, such as LiF, CsF, and CaF_2, have also been introduced as the cathode interfacial layer (CIL).[17,26–29] Although these metal fluorides are nonconducting, these ultrathin CILs can significantly improve the performance of OPVs.

The mechanism of action of the metal fluorides placed between the metal electrode and active layer has been extensively investigated and can be explained with the following three models: reaction, dipole, and tunneling. The reaction model states that the evaporated aluminum metal electrode reacts with the ultrathin fluorides, following which low-WF metal atoms are released from the latter. The free metal atoms are doped into the active layer, which results in the lowering of the effective WF of the cathode and, consequently, effective extraction of photogenerated electrons.[30] The dipole model demonstrates that electron transfer occurs between fluorides and the metal electrode, which decreases the effective WF of the cathode through a decrease of the surface potential of the electrode, resulting in improved electron injection.[26,28] The tunneling model reveals that inserting an ultrathin insulating metal fluoride between the metal electrode and active layer leads to a reduction of the band bending of the active layer; this results in a decreased effective barrier, which enhances the effective electron tunneling.[31] Although the exact mechanism governing the role of ultrathin metal fluorides in OPV devices is still under debate, much evidence suggests that the mechanism operating at the fluoride/metal interface cannot be explained by any one model, but rather is explicable by a combination of two

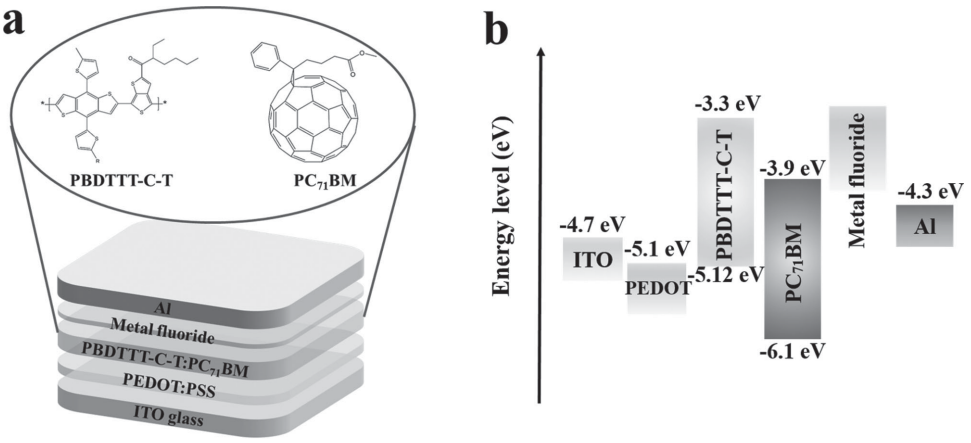

Figure 1. a) The schematic architecture of OPVs based on PBDTTT-C-T:$PC_{71}BM$ blend. b) The energy level alignment of the materials in OPVs used in this work.

or more models. Moreover, there is still lack of proper understanding of some aspects of the metal fluoride CILs, such as their effects on the properties of the OPV devices; moreover, the possibility of developing a method to estimate the effects of metal fluoride CILs on OPV performance prior to performing actual experiments has seldom been explored.

In this paper, we discuss the effects of CILs made of different metal fluorides, including lithium fluoride (LiF), magnesium fluoride (MgF_2), barium fluoride (BaF_2), strontium fluoride (SrF_2), aluminum fluoride (AlF_3), zirconium fluoride (ZrF_4), and cerium fluoride (CeF_3), on the performance of OPV devices. This is the first report on using SrF_2 and CeF_3 as CILs in OPV devices. The SrF_2 device exhibited the highest PCE of 7.17%, which is 9% higher than the PCE of the control device with 10 Å LiF as the interfacial layer. Moreover, the device performance was found to be related to the WF of the corresponding pure metal in the fluoride (denoted as WF_{MIF}). A low WF_{MIF} corresponds to a high open-circuit voltage (V_{OC}) and a high fill factor (FF), and thus an improved PCE. The mechanism governing the role of ultrathin metal fluorides in OPV devices was investigated in detail, which reveals that the mechanism acting at the fluoride/metal interface can be explained by a combination of the reaction and dipole models.

2. Results and Discussion

Figure 1 shows the device structure and the energy-level alignment of the materials used in this work. The widely used indium-tin oxide (ITO)/poly(3,4-ethylene dioxythiophene)–polystyrene

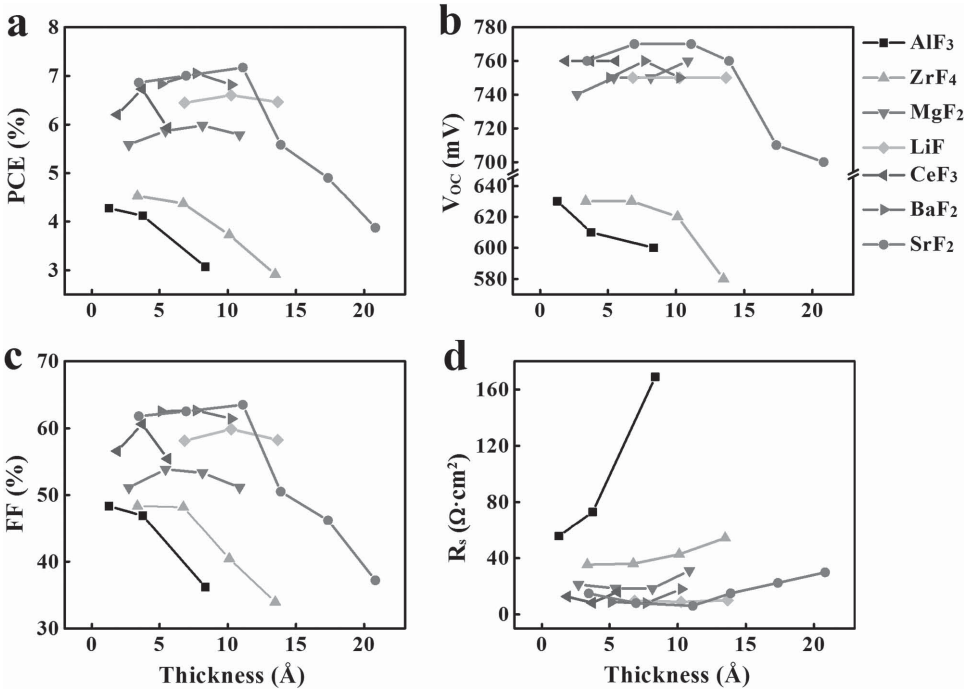

Figure 2. a) PCE, b) V_{OC}, c) FF, and d) R_s of devices with metal fluoride CILs of different thicknesses.

sulfonic acid (PEDOT:PSS) was utilized as the anode; polymer photovoltaic materials poly[4,8-bis-substituted-benzo[1,2-b:4,5-b′]dithiophene-2,6-diyl-alt-4-substituted-thieno[3,4-b]thiophene-2,6-diyl] (PBDTTT-C-T) and [6,6]-phenyl C71-butyric acid methyl ester ($PC_{71}BM$) were introduced as the donor and acceptor, respectively; and different fluorides combined with Al were used as the cathode for electron extraction.

Figure 2 shows device parameters including V_{OC}, short-circuit current density (J_{SC}), FF, and PCE as a function of the thickness of fluoride for the different fluoride-based devices. The detailed performance parameters of these OPV devices are shown in Figures S1 and S2 and Tables S1–S7 in the Supporting Information. The devices with different fluoride interfacial layers exhibit optimal performance at different fluoride thicknesses; the optimal thicknesses of AlF_3, ZrF_4, MgF_2, LiF, CeF_3, BaF_2, and SrF_2 are 1, 3, 8, 10, 6, 8, and 11 Å, respectively. Here, we take SrF_2 as an example to explain the device performance (V_{OC} and FF) depending on the fluoride thickness. SrF_2 deposited under high vacuum conditions follows the island-growth mode on the surface of the active layer (Figure S4, Supporting Information), which is similar to the growth of BaF_2.[30,32] When the nominal thickness of SrF_2 is less than that of single-coverage layer, only part of SrF_2 layer covers on the polymeric photoactive layer. With the increase of the nominal thickness of SrF_2 layer, the SrF_2 grows from little island to large island, and gradually forms a single-coverage layer, resulting in an increased V_{OC} and PCE, and a decreased series resistance (R_s). As the SrF_2 thickness increases, the average root-mean-square roughness increases from 0.965 nm (active layer surface without SrF_2) to 1.147 nm (active layer surface with 11 Å SrF_2), which proves the island growth of SrF_2 layer (Figure S4b, Supporting Information). However, the FF and the PCE decrease abruptly, and R_s increases as the thickness of the SrF_2 layer exceeds that of a single-coverage layer, which is ascribed to the insulating nature of SrF_2. The optimized current density–voltage (J–V) characteristics of each device under illumination and in the dark are summarized in **Figure 3**a,b, respectively, and the device parameters are listed in **Table 1**. The V_{OC} of the devices increases from 630.00 to 770.03 mV in the following order: AlF_3 < ZrF_4 < MgF_2 < LiF < CeF_3 < BaF_2 < SrF_2. Moreover, the PCE of these devices also increases from 4.28% for the AlF_3-based device to 7.17% for the SrF_2-based device.

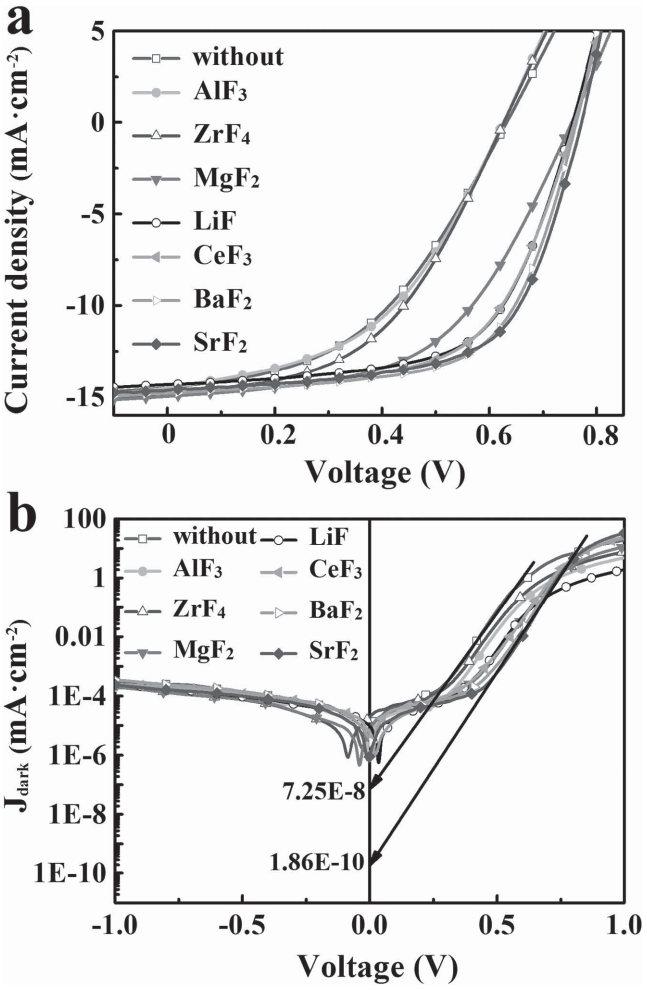

Figure 3. J–V characteristics of the OPVs with different optimal fluoride thicknesses a) under AM 1.5G irradiation at 100 mW cm^{-2} and b) in the dark.

V_{OC} depends on temperature, light intensity, material microstructure, and the WF of electrode.[39] Therefore, to explore the WFs of different fluoride-based electrodes, ultraviolet photoelectron spectroscopy (UPS) measurements were carried out, the results of which are shown in **Figure 4**a. The calculated WFs

Table 1. PCE, V_{OC}, J_{SC}, FF, R_s, R_{sh}, J_0, and n of OPVs with different optimal thicknesses of CILs, WF_{MIF} of CILs, and effective WFs of cathodes.

CIL	Optimal thickness [Å]	WF_{MIF} [eV]	Effective WF of cathodes [eV]	V_{OC} [mV]	J_{SC} [mA cm^{-2}]	FF [%]	R_s [Ω cm^2]	R_{sh} [MΩ cm^2]	PCE [%]	J_0 [mA cm^{-2}]	n [V]
Without[a)]	0	–	4.30	630.03	14.53	45.57	55.99	4.77	4.17	7.25×10^{-8}	1.61
AlF_3	1	4.30[33]	4.25	630.00	14.47	48.35	55.65	2.61	4.27	6.75×10^{-8}	1.61
ZrF_4	3	4.05[34]	4.12	630.04	14.86	48.38	35.40	2.95	4.53	6.49×10^{-8}	1.59
MgF_2	8	3.66[35]	3.85	750.05	14.96	53.31	18.41	2.53	5.98	6.65×10^{-9}	1.58
LiF[a)]	10	2.90[35]	3.11	750.07	14.70	59.87	8.95	1.75	6.60	3.44×10^{-9}	1.56
CeF_3	6	2.90[36]	3.06	760.02	14.61	60.61	8.27	1.73	6.73	1.87×10^{-9}	1.51
BaF_2	8	2.70[37]	2.95	760.04	14.81	62.65	8.05	1.93	7.05	9.06×10^{-10}	1.48
SrF_2	11	2.59[38]	2.90	770.03	14.63	63.50	6.10	5.32	7.17	1.86×10^{-10}	1.32

[a)]Control device

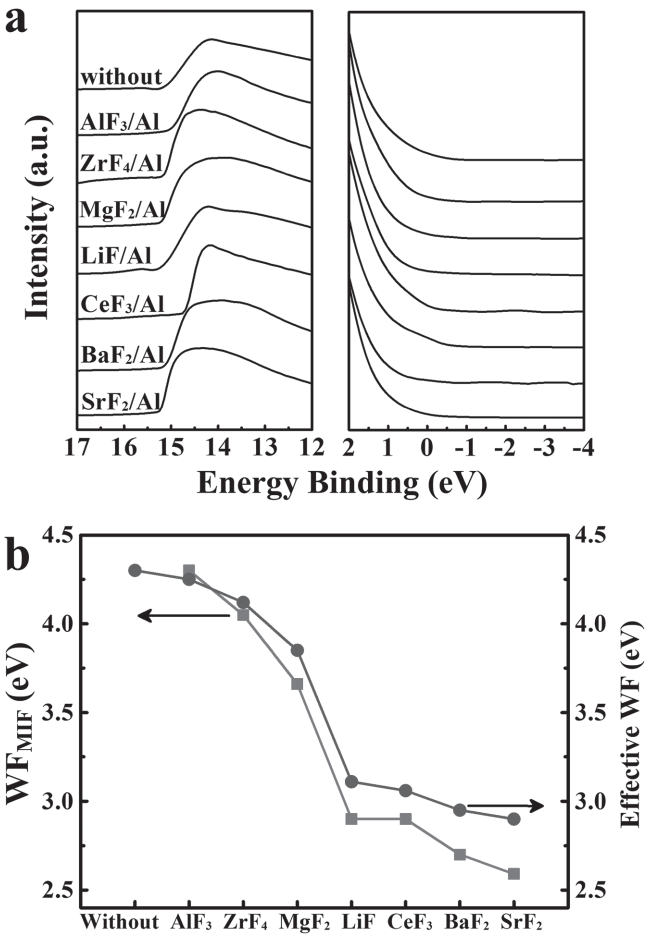

Figure 4. a) UPS spectra of Al, AlF_3/Al, ZrF_4/Al, MgF_2/Al, LiF/Al, CeF_3/Al, BaF_2/Al, and SrF_2/Al. b) WF_{MIF} of each fluoride CIL and the effective WFs of different cathodes (without or with fluoride CILs).

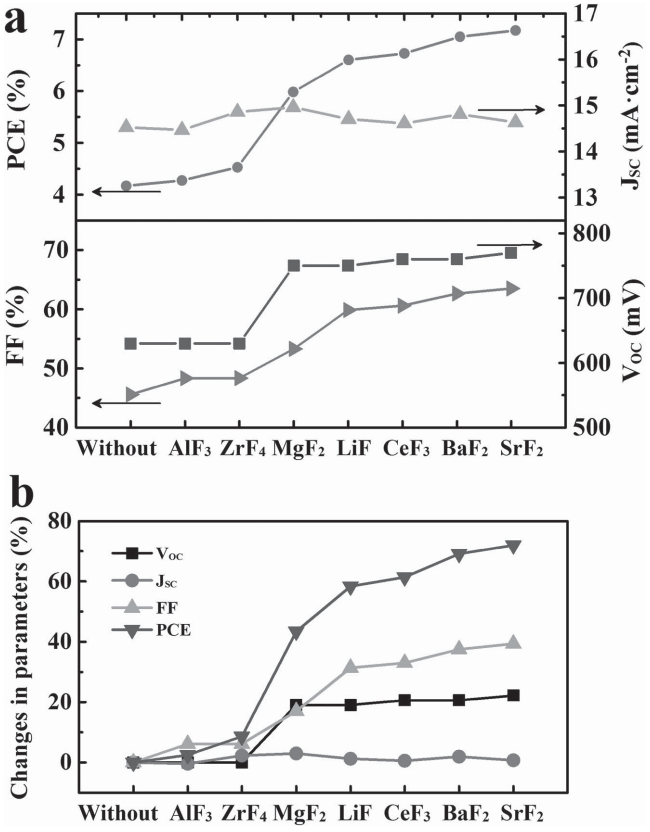

Figure 5. a) PCE, J_{SC}, V_{OC}, and FF of the OPVs with CILs of different optimal thicknesses under simulated solar AM 1.5G illumination at an intensity of 100 mW cm^{-2}. b) Changes in V_{OC}, J_{SC}, FF, and PCE when compared with a device without a CIL.

of these electrodes are also listed in Table 1 and the detailed UPS data are provided in Table S8 (Supporting Information). The WF decreases gradually from 4.25 eV for the AlF_3-based electrode to 2.90 eV for the SrF_2-based electrode, thus exhibiting an opposite trend compared with V_{OC}. For the AlF_3- or ZrF_4-based electrode, the WF (4.25 or 4.12 eV) is higher than the lowest unoccupied molecular orbital (LUMO) level of the acceptor $PC_{71}BM$ (3.9 eV); thus, nonohmic contacts are formed, which subsequently lead to a decreased V_{OC}. For the other fluoride-based electrodes, the WFs are all below the LUMO level of $PC_{71}BM$. Thus, ohmic contacts are formed, with the electrode WF being pinned to the LUMO level of the acceptor, which enables achieving almost constant V_{OC} in MgF_2-, LiF-, CeF_3-, BaF_2-, and SrF_2-based devices.

According to the reaction model, the displacement reaction can be expressed as follows

$$3MF_x + xAl \rightarrow 3M + xAlF_3 \quad (1)$$

where MF_x is the metal fluoride. According to this equation, low-WF metals, such as Zr, Mg, Li, Ce, Ba, and Sr will be generated at the fluoride/aluminum interface, which will lower the cathode WF. The WFs of pure metals in the fluorides (WF_{MIF}) are listed in Table 1. The variation tendency of the WF_{MIF} is similar to that of the cathode WF measured by UPS (Figure 4b).[40,41] Therefore, it is concluded that the WF of the fluoride-based cathode can be determined from the corresponding WF_{MIF}, which affects the V_{OC} of the OPV devices.

Figure 5a shows the evolution of device parameters, including PCE, J_{SC}, V_{OC}, and FF, for different metal fluoride interfacial layers. J_{SC} changes slightly, whereas V_{OC} and FF exhibit noticeable changes for different fluoride-based cathodes. Figure 5b shows the changes of these parameters relative to those of the control device without a CIL. Compared with the control device, the SrF_2-based device shows an increase of 22% and 39% in V_{OC} and FF, respectively, with a 72% increase in PCE. This indicates that the enhanced PCE of the fluoride-based device can be attributed not only to the increased V_{OC}, but also to the improved FF, which is an important parameter that is influenced by R_s, shunt resistance (R_{sh}), saturation dark current density (J_0), and ideality factor (n).[42]

These parameters were extracted from the J–V curves in the dark (Figure 3b) and are listed in Table 1. The FF increases from 48.35% for the AlF_3-based device to 63.50% for the SrF_2-based device, and shows a similar increasing tendency as V_{OC}, i.e., $AlF_3 < ZrF_4 < MgF_2 < LiF < CeF_3 < BaF_2 < SrF_2$. R_s decreases from 55.65 Ω cm^2 for the AlF_3-based device to 6.10 Ω cm^2 for the SrF_2-based device in the opposite order. R_{sh} fluctuates on

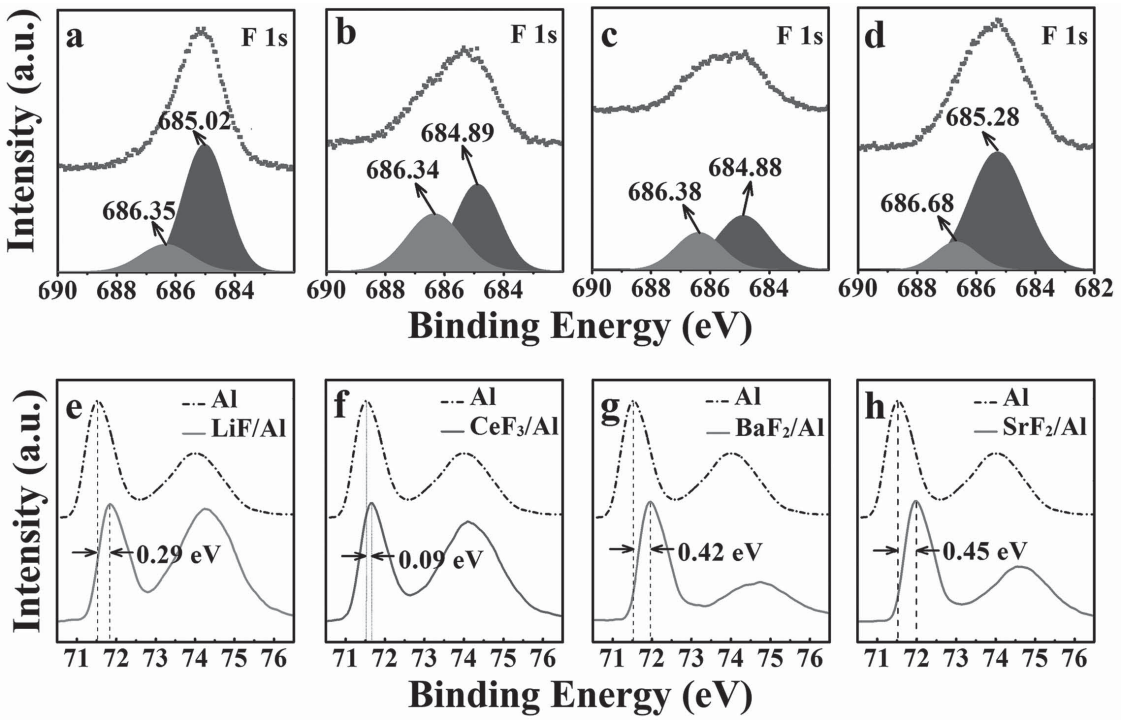

Figure 6. a–d) F 1s and e–h) Al 2p peaks in the XPS spectra of LiF/Al, CeF_3/Al, BaF_2/Al, and SrF_2/Al cathodes, respectively.

the same order of magnitude in these devices and reaches the maximum value of 5.32 MΩ cm^2 for the SrF_2-based device. Moreover, according to the dark *J*–*V* curves, J_0 and *n* can be extracted by fitting the data into the Shockley equation [39,43,44]

$$J = J_0\left[\exp\left(\frac{q(V - JR_s)}{nk_BT} - 1\right)\right] + \frac{V - JR_s}{R_{sh}} - J_{ph} \quad (2)$$

where *q* is the elementary charge, *T* is temperature, and k_B is the Boltzmann constant. Here, the ideality factor *n*, which is an indicator of the geminate recombination during transport and bimolecular recombination during charge collection, is an important parameter for evaluating the quality of OPV devices.[42,45] For the same V_{OC}, a device with a lower *n* will have a higher FF.[42] As can be seen in Table 1, the value of *n* decreases gradually in the order of AlF_3 > ZrF_4 > MgF_2 > LiF > CeF_3 > BaF_2 > SrF_2, achieving a minimum value of 1.32 for the SrF_2-based device; this indicates the SrF_2-based device has the best transport and collection processes. According to the Shockley equation, J_0 is related to V_{OC}, which can be expressed as[44]

$$V_{OC} = \frac{nk_BT}{q}\ln\left(\frac{J_{SC}}{J_0}\right) \quad (3)$$

This equation indicates a smaller J_0 means a higher V_{OC}. As shown in Table 1, J_0 decreases in the following order: AlF_3 > ZrF_4 > MgF_2 > LiF > CeF_3 > BaF_2 > SrF_2, with the SrF_2-based device showing the lowest J_0 of 1.86×10^{-10} mA cm^{-2}, which is approximately two orders of magnitude lower than that of the AlF_3-based device. According to Equation (3), V_{OC} will increase in the order, AlF_3 < ZrF_4 < MgF_2 < LiF < CeF_3 < BaF_2 < SrF_2; this is verified experimentally, as shown in Figure 3 and Table 1.

In order to explore the mechanism related to the role of different metal fluorides in OPV devices, we performed X-ray photoelectron spectroscopy (XPS) measurements on LiF/Al, CeF_3/Al, BaF_2/Al, and SrF_2/Al cathodes; the F 1s and Al 2p peaks are shown in **Figure 6**. In the F 1s spectra in Figure 6a–d, two obvious peaks at approximately 685 and 686 eV were found after detailed peak fitting. The peaks at 685.02 eV (Figure 6a), 684.89 eV (Figure 6b), 684.88 eV (Figure 6c), and 685.28 eV (Figure 6d) are attributed to LiF,[46–48] CeF_3,[49,50] BaF_2,[51,52] and SrF_2,[53,54] respectively. The peaks at 686.35 eV (Figure 6a), 686.34 eV (Figure 6b), 686.38 eV (Figure 6c), and 686.68 eV (Figure 6d) are due to AlF_3.[55,56] The presence of AlF_3 in all of these four cathodes indicates the occurrence of a displacement reaction between individual fluorides and Al; this indirectly confirms that the effective WF of the fluoride-based cathode is reduced as a result of the generation of the low-WF metal, such as Li, Ce, Ba, or Sr.

In the Al 2p spectra shown in Figure 6e–h, the pure Al film shows two peaks at approximately 71.5 and 74 eV, which are attributed to metal Al and aluminum oxide, respectively. However, for the Al film with the ultrathin LiF, CeF_3, BaF_2, and SrF_2 layers, the two peaks show a shift by 0.29, 0.09, 0.42, and 0.45 eV toward high binding energy, respectively. This indicates that electrons are lost from Al at the fluoride/aluminum interface, and a dipole that is directed toward the active layer is formed, which accelerates the extraction of electrons at the cathode. A larger peak shift implies the presence of a stronger dipole at the fluoride/aluminum interface, resulting in a faster charge collection and a reduced bimolecular recombination at the electrode, and thus a lower n of the OPV device. Among the four fluoride interfaces, SrF_2/Al exhibits the largest dipole, thus indicating the minimum bimolecular recombination at this interface;

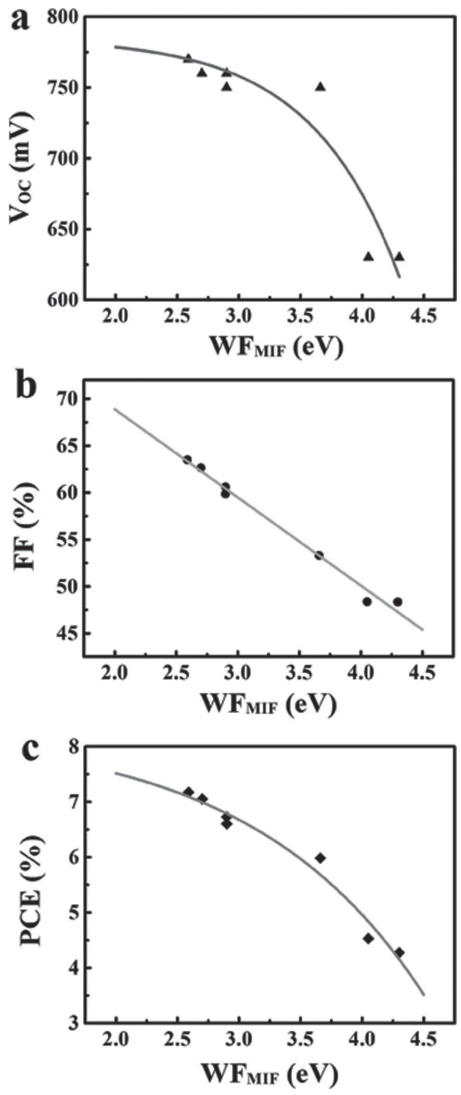

Figure 7. Fitted curves of device parameters as a function of WF_{MIF}: a) V_{OC}, b) FF, and c) PCE.

moreover, this means that the minimum n will be achieved for the SrF_2-based device, which is consistent with the calculated n in Table 1. Therefore, the highest FF could be achieved with the SrF_2-based device.

In light of the above discussion, we plot the correlation between device properties and different metal fluorides in **Figure 7**. The figure shows that as WF_{MIF} decreases from 4.3 to 2.59 eV, the fitted V_{OC} curve increases exponentially, while FF increases linearly, resulting in an exponential increase of PCE. The correlation between device properties and WF_{MIF} may be extended to other metal fluoride CILs in OPVs. Thus, this work provides a simple method to estimate the effect of a metal fluoride CIL on OPV performance prior to performing experiments.

3. Conclusions

In summary, we have introduced different metal fluoride CILs in OPVs. The V_{OC} and FF of the device were found to increase with the decrease of WF_{MIF} in the following order: $AlF_3 < ZrF_4 < MgF_2 < LiF < CeF_3 < BaF_2 < SrF_2$. The SrF_2-based device showed the highest PCE of 7.17%, with the highest V_{OC} of 770 mV and the highest FF of 63.5%. The XPS studies of the fluoride cathodes confirmed the presence of a displacement reaction and an interfacial dipole at the fluoride/aluminum interface, which led to reduced effective WFs of cathodes and improved charge collection. As a result, an improved PCE was achieved together with an increased V_{OC} and FF. These results indicate that the mechanism operating at the fluoride/metal interface can be explained through a combination of the reaction and dipole models. This report will provide a useful reference for investigating the mechanism at the fluoride/metal interface in OPVs, estimating the effect of a metal fluoride CIL on OPV performance, and selection of interfacial layers to realize efficient OPVs in a simple way.

4. Experimental Section

Device Fabrication: The ITO coated glass anode was cleaned with acetone, alcohol, and deionized water in an ultrasonic bath and then placed in a vacuum drying oven to remove moisture. Next, the ITO substrates were treated with ultraviolet ozone for 15 min and immediately coated with PEDOT:PSS (Baytron P AI 4083, 30 nm). Subsequently, the samples were heated for 10 min at 120 °C on a hot plate to eliminate residual water and transferred into an N_2 glove box. A blend of a low bandgap conjugated polymer, PBDTTT-C-T, and $PC_{71}BM$ (American Dye) was spin-coated onto the samples from dichlorobenzene for use as the active layer (800 rpm, ca. 100 nm). A small amount (3 vol%) of a high boiling point additive, 1,8-diiodooctane (DIO, Sigma-Aldrich), was used to optimize the morphology of the active layer.[57] Finally, metal fluorides of different thicknesses and Al (100 nm) were thermally deposited at a pressure of 2.5×10^{-4} Pa. The active area of the OPV devices was 0.12 cm^2. All measurements were performed in air without encapsulation.

Characterization: The *J–V* characteristics of OPVs were measured using a computer-controlled Keithley 2611 source meter under AM 1.5G illumination from a calibrated solar simulator with an irradiation intensity of 100 mW cm^{-2} and in the dark. UPS spectra were obtained using a Thermo ESCALAB 250 surface analysis system equipped with a helium discharge lamp at $h\nu$ = 21.22 eV. XPS studies were carried out using a Thermo ESCALAB 250 instrument with Al Kα X-rays ($h\nu$ = 1486.6 eV) to investigate the surface properties. The C 1s peak at 284.5 eV was considered the standard for all charge shift corrections during the peak fitting process. The absorption spectra of the active layer were recorded on a Shimadzu UV-3101PC UV–vis–NIR scanning spectrophotometer. External quantum efficiency measurements were performed with a lock-in amplifier at a chopping frequency of 20 Hz under illumination with monochromatic light from a Xenon lamp. Film thicknesses were measured with an Ambios XP-1 surface profiler. Atomic force microscopy measurements were performed on an SA400HV instrument with a SPI3800N controller (Seiko Instruments Industry, Co., Ltd).

Supporting Information

Supporting Information is available from the Wiley Online Library or from the author.

Acknowledgements

This work was supported by the CAS Innovation Program, the National Science Foundation of China Grant Nos. 61106057 and 6140031454, the Jilin Province Science and Technology Research Project Nos.

20140520119JH and 20150101039JC, and Project supported by State Key Laboratory of Luminescence and Applications.

Received: July 12, 2015
Revised: September 11, 2015
Published online: October 27, 2015

[1] G. Yu, J. Gao, J. Hummelen, F. Wudl, A. Heeger, *Science* **1995**, *270*, 1789.
[2] F. Padinger, R. S. Rittberger, N. S. Sariciftci, *Adv. Funct. Mater.* **2003**, *13*, 85.
[3] S. R. Forrest, *Nature* **2004**, *428*, 911.
[4] M. C. Scharber, D. Mühlbacher, M. Koppe, P. Denk, C. Waldauf, A. J. Heeger, C. J. Brabec, *Adv. Mater.* **2006**, *18*, 789.
[5] B. H. Lee, S. H. Park, H. Back, K. Lee, *Adv. Funct. Mater.* **2011**, *21*, 487.
[6] J. You, L. Dou, K. Yoshimura, T. Kato, K. Ohya, T. Moriarty, K. Emery, C.-C. Chen, J. Gao, G. Li, *Nat. Commun.* **2013**, *4*, 1446.
[7] B. Park, S. H. Yun, C. Y. Cho, Y. C. Kim, J. C. Shin, H. G. Jeon, Y. H. Huh, I. Hwang, K. Y. Baik, Y. I. Lee, H. S. Uhm, G. S. Cho, E. H. Choi, *Light: Sci. Appl.* **2014**, *3*, e222.
[8] F. C. Krebs, N. Espinosa, M. Hösel, R. R. Søndergaard, M. Jørgensen, *Adv. Mater.* **2014**, *26*, 29.
[9] C. Dyer-Smith, I. A. Howard, C. Cabanetos, A. El Labban, P. M. Beaujuge, F. Laquai, *Adv. Energy Mater.* **2015**, *5*, 1401778.
[10] B. Roth, G. A. dos Reis Benatto, M. Corazza, R. R. Søndergaard, S. A. Gevorgyan, M. Jørgensen, F. C. Krebs, *Adv. Energy Mater.* **2015**, *5*, 1401912.
[11] S.-H. Liao, H.-J. Jhuo, P.-N. Yeh, Y.-S. Cheng, Y.-L. Li, Y.-H. Lee, S. Sharma, S.-A. Chen, *Sci. Rep.* **2014**, *4*, 6813.
[12] Y. Liu, J. Zhao, Z. Li, C. Mu, W. Ma, H. Hu, K. Jiang, H. Lin, H. Ade, H. Yan, *Nat. Commun.* **2014**, *5*, 5293.
[13] Z. He, B. Xiao, F. Liu, H. Wu, Y. Yang, S. Xiao, C. Wang, T. P. Russell, Y. Cao, *Nat, Photon.* **2015**, *9*, 174.
[14] C. He, Q. He, Y. He, Y. Li, F. Bai, C. Yang, Y. Ding, L. Wang, J. Ye, *Sol. Energy Mater. Sol. Cells* **2006**, *90*, 1815.
[15] M. O. Reese, M. S. White, G. Rumbles, D. S. Ginley, S. E. Shaheen, *Appl. Phys. Lett.* **2008**, *92*, 053307.
[16] K.-G. Lim, M.-R. Choi, H.-B. Kim, J. H. Park, T.-W. Lee, *J. Mater. Chem.* **2012**, *22*, 25148.
[17] J. H. Park, T. W. Lee, B. D. Chin, D. H. Wang, O. O. Park, *Macromol. Rapid Commun.* **2010**, *31*, 2095.
[18] J. Y. Kim, S. H. Kim, H. H. Lee, K. Lee, W. Ma, X. Gong, A. J. Heeger, *Adv. Mater.* **2006**, *18*, 572.
[19] K. Lee, J. Y. Kim, S. H. Park, S. H. Kim, S. Cho, A. J. Heeger, *Adv. Mater.* **2007**, *19*, 2445.
[20] Y. Jouane, S. Colis, G. Schmerber, P. Kern, A. Dinia, T. Heiser, Y. A. Chapuis, *J. Mater. Chem.* **2011**, *21*, 1953.
[21] Y. Jouane, S. Colis, G. Schmerber, C. Leuvrey, A. Dinia, P. Lévêque, T. Heiser, Y.-A. Chapuis, *J. Mater. Chem.* **2012**, *22*, 1606.
[22] P. S. Mbule, T. H. Kim, B. S. Kim, H. C. Swart, O. M. Ntwaeaborwa, *Sol. Energy Mater. Sol. Cells* **2013**, *112*, 6.
[23] X. Li, F. Xie, S. Zhang, J. Hou, W. C. H. Choy, *Light: Sci. Appl.* **2015**, *4*, e273.
[24] S. Shao, J. Liu, B. Zhang, Z. Xie, L. Wang, *Appl. Phys. Lett.* **2011**, *98*, 203304.
[25] J. Kim, G. Kim, Y. Choi, J. Lee, S. H. Park, K. Lee, *J. Appl. Phys.* **2012**, *111*, 114511.
[26] C. J. Brabec, S. E. Shaheen, C. Winder, N. S. Sariciftci, P. Denk, *Appl. Phys. Lett.* **2002**, *80*, 1288.
[27] S. K. M. Jönsson, E. Carlegrim, F. Zhang, W. R. Salaneck, M. Fahlman, *Jpn. J. Appl. Phys.* **2005**, *44*, 3695.
[28] X. Jiang, H. Xu, L. Yang, M. Shi, M. Wang, H. Chen, *Sol. Energy Mater. Sol. Cells* **2009**, *93*, 650.
[29] L. M. Chen, Z. Xu, Z. Hong, Y. Yang, *J. Mater. Chem.* **2010**, *20*, 2575.
[30] T. W. Lee, M. G. Kim, S. H. Park, S. Y. Kim, O. Kwon, T. Noh, J. J. Park, T. L. Choi, J. H. Park, B. D. Chin, *Adv. Funct. Mater.* **2009**, *19*, 1863.
[31] V. D. Mihailetchi, P. W. M. Blom, J. C. Hummelen, M. T. Rispens, *J. Appl. Phys.* **2003**, *94*, 6849.
[32] K. G. Lim, M. R. Choi, J. H. Kim, D. H. Kim, G. H. Jung, Y. Park, J. L. Lee, T. W. Lee, *Chem. Sus. Chem.* **2014**, *7*, 1125.
[33] E. Kymakis, G. Amaratunga, *Appl. Phys. Lett.* **2002**, *80*, 112.
[34] P. K. Baumann, R. J. Nemanich, *J. Appl. Phys.* **1998**, *83*, 2072.
[35] L. S. Hung, C. W. Tang, M. G. Mason, *Appl. Phys. Lett.* **1997**, *70*, 152.
[36] M. Y. Chan, S. L. Lai, M. K. Fung, C. S. Lee, S. T. Lee, *J. Appl. Phys.* **2004**, *95*, 5397.
[37] X. Gong, M. Tong, F. G. Brunetti, J. Seo, Y. Sun, D. Moses, F. Wudl, A. J. Heeger, *Adv. Mater.* **2011**, *23*, 2272.
[38] S. Y. Kim, D. G. Moon, C. J. Lee, J. I. Han, *Thin Solid Films* **2009**, *517*, 2035.
[39] B. Qi, J. Wang, *J. Mater. Chem.* **2012**, *22*, 24315.
[40] Y. Park, V. Choong, Y. Gao, B. Hsieh, C. Tang, *Appl. Phys. Lett.* **1996**, *68*, 2699.
[41] W.-B. Zhang, Y. Tu, H.-J. Sun, K. Yue, X. Gong, S. Z. D. Cheng, *Sci. China Chem.* **2012**, *55*, 749.
[42] D. Gupta, S. Mukhopadhyay, K. Narayan, *Sol. Energy Mater. Sol. Cells* **2010**, *94*, 1309.
[43] W. J. Potscavage, S. Yoo, B. Kippelen, *Appl. Phys. Lett.* **2008**, *93*, 193308.
[44] B. Qi, Z. G. Zhang, J. Wang, *Sci. Rep.* **2015**, *5*, 7803.
[45] G. Wetzelaer, M. Kuik, M. Lenes, *P. Blom. Appl. Phys. Lett.* **2011**, *99*, 153506.
[46] D. Dambournet, K. W. Chapman, P. J. Chupas, R. E. Gerald, 2nd, N. Penin, C. Labrugere, A. Demourgues, A. Tressaud, K. Amine, *J. Am. Chem. Soc.* **2011**, *133*, 13240.
[47] F. Ding, W. Xu, X. Chen, J. Zhang, Y. Shao, M. H. Engelhard, Y. Zhang, T. A. Blake, G. L. Graff, X. Liu, J.-G. Zhang, *J. Phys. Chem. C* **2014**, *118*, 4043.
[48] N. Dupré, J.-F. Martin, J. Oliveri, P. Soudan, A. Yamada, R. Kanno, D. Guyomard, *J. Power Sources* **2011**, *196*, 4791.
[49] S. Daniele, L. G. Hubert-Pfalzgraf, M. Perrin, *Polyhedron* **2002**, *21*, 1985.
[50] L. Wang, M. Zhang, X. Wang, W. Liu, *Mater. Res. Bull.* **2008**, *43*, 2220.
[51] R. Velmurugan, B. Krishnakumar, M. Swaminathan, *Mater. Sci. Semicond. Process.* **2014**, *27*, 654.
[52] A. Zakutayev, J. Tate, H. A. S. Platt, D. A. Keszler, C. Hein, T. Mayer, A. Klein, W. Jaegermann, *J. Appl. Phys.* **2010**, *107*, 103713.
[53] L. P. Dai, G. J. Zhang, S. Y. Wang, Z. Q. Zhong, *Adv. Mater. Res.* **2011**, *415*, 1964.
[54] M. Yagoub, H. Swart, L. Noto, P. Bergman, E. Coetsee, *Materials* **2015**, *8*, 2361.
[55] J.-S. Luo, H.-M. Lo, J. D. Russell, presented at 31st Int. Symp. Testing Failure Anal. (ISTFA) 2005, San Jose, CA, USA, November 2005.
[56] M. Watanabe, Y. Mori, T. Ishikawa, T. Iida, K. Akiyama, K. Sawabe, K. Shobatake, *Appl. Surf. Sci.* **2003**, *217*, 82.
[57] X. Guo, M. Zhang, W. Ma, L. Ye, S. Zhang, S. Liu, H. Ade, F. Huang, J. Hou, *Adv. Mater.* **2014**, *26*, 4043.